Title	Seasonal and interannual variability in the temperature structure around the tropical tropopause and its relationship with convective activities
Author(s)	Nishimoto, Eriko; Shiotani, Masato
Citation	Journal of Geophysical Research (2012), 117
Issue Date	2012
URL	http://hdl.handle.net/2433/153298
Right	©2012. American Geophysical Union.
Type	Journal Article
Textversion	author

JOURNAL OF GEOPHYSICAL RESEARCH, VOL. ???, XXXX, DOI:10.1029/,

Seasonal and interannual variability in the temperature structure around the tropical tropopause and its relationship with convective activities

Eriko Nishimoto[1] and Masato Shiotani[1]

E. Nishimoto, Research Institute for Sustainable Humanosphere, Kyoto University, Gokasho, Uji, Kyoto 611-0011, Japan. (eriko@rish.kyoto-u.ac.jp)

M. Shiotani, Research Institute for Sustainable Humanosphere, Kyoto University, Gokasho, Uji, Kyoto 611-0011, Japan. (shiotani@rish.kyoto-u.ac.jp)

[1]Research Institute for Sustainable Humanosphere, Kyoto University, Gokasho, Uji, Japan.

Abstract. Seasonal and interannual variability in the tropical tropopause temperatures and its relationship with convective activities are examined by using the ECMWF 40-year reanalysis data and NOAA/OLR data. Low temperatures generally occur over the equator in the Eastern Hemisphere and extend north-westward and south-westward in the subtropics to form a horseshoe-shaped structure. Because this structure resembles a stationary wave response known as the Matsuno-Gill pattern, which is a superposition of the Rossby and Kelvin responses, the two preliminary indices are defined to represent the two responses. The horseshoe-shaped structure index is then calculated from the two indices. The seasonal cycle in the horseshoe-shaped structure index is significantly related to that observed in convective activities adjacent to three monsoon regions: the South Asian monsoon (SoAM) and the North Pacific monsoon (NPM) areas during the northern summer and the Australian monsoon (AUM) area during the southern summer. The convective activities in the SoAM and NPM areas individually influence the horseshoe-shaped structure. During the northern summer, interannual variation in the horseshoe-shaped structure index in the NPM area is related to that observed in convective activities associated with the El Niño-Southern Oscillation (ENSO) cycle with about a half-year time lag. In the SoAM area, the variation is mainly controlled by isolated high temperatures, which are surrounded by the horseshoe-shaped temperature structures and are not related to convective activities. During the southern summer, the horseshoe-shaped structure index is related

to convective anomalies associated with the ENSO cycle, shifting eastward in El Niño years.

1. Introduction

The tropical tropopause (∼100 hPa) is the primary exchange region of mass and chemical species between the troposphere and stratosphere. In particular, the tropical tropopause temperature is one of the most important factors that control aridity of air in the stratosphere [e.g. *Fueglistaler et al.*, 2009]. Water vapor in the stratosphere influences variability and recovery of the ozone layer through its radiative and photochemical nature [e.g., *Kley et al.*, 2000]. Hence, spatial and temporal variations in the tropical tropopause temperature have been intensively investigated by a number of studies [e.g., *Seidel et al.*, 2001; *Hartmann*, 2007].

Newell and Gould-Stewart [1981] surveyed the temperature distribution at 100 hPa using global data from a radiosonde network, and showed that temperatures lower than the zonal average are found over the Indian Ocean during the northern summer and over the Western Pacific during the southern summer. *Highwood and Hoskins* [1998] analyzed the European Centre for Medium-Range Weather Forecasts (ECMWF) data to show that these low temperatures in the tropics extend north-westward and south-westward toward the subtropics, forming a horseshoe-shaped structure, which usually accompanies convective activities (Figure 1).

This horseshoe-shaped structure resembles the stationary wave response known as the Matsuno-Gill pattern. *Matsuno* [1966] investigated several equatorial wave modes in a shallow-water equation, and *Gill* [1980] showed that heating near the equator produces a characteristic wave structure in wind and pressure fields, which was later named the Matsuno-Gill pattern. This wave form can be described as a combined structure of two types: one is located in the eastern part and represents a Kelvin wave confined around the equator with no meridional velocity, and the other is in the western part and represents a Rossby wave with a pair of symmetric circulations in the subtropics.

The Matsuno-Gill response in the tropopause temperature has been demonstrated using multiple-layer models by *Highwood and Hoskins* [1998] and *Norton* [2006]. They also showed that wind and pressure fields have a corresponding pattern to satisfy the hydrostatic relationship; anticyclonic circulations exist in the upper troposphere subtropics, while cyclonic circulations in the lower troposphere subtropics. Using ECMWF 40-year reanalysis (ERA-40) data, *Dima and Wallace* [2007] estimated the annual-mean temperature fields in the tropics from geopotential height data through the hypsometric equation, and found the horseshoe-shaped structure with low temperatures over the Western Pacific in the 150-70 hPa layer. *Hatsushika and Yamazaki* [2003] investigated the transport process through the tropical tropopause in an atmospheric general circulation model (AGCM) and revealed that the cold tropopause temperatures and the upper tropospheric circulations characterized by the Matsuno-Gill pattern play an important role in the dehydration process.

Randel and Park [2006] and *Park et al.* [2007] used National Centers for Environmental Prediction/National Center for Atmospheric Research (NCEP/NCAR) reanalysis and outgoing longwave radiation (OLR) data, and showed that low tropopause temperatures presented in the Eastern Hemisphere during the northern summer are coupled to convective activities adjacent to the Asian monsoon region. However, the spatial and temporal variability of the horseshoe-shaped structure and the quantitative evaluation of its relationship with convective activities are not clear yet.

Another aspect of the quasi-stationary temperature fields forming a horseshoe-shaped structure around the tropopause was surveyed by *Nishi et al.* [2010]. They used ERA-40 data to show that isolated high temperatures exist around 60°E and are surrounded by the horseshoe-shaped low temperature structure during the northern summer. In addition, they pointed out that the warm anomaly magnitude was small in the El Niño years (1987 and 1997).

Major convective activities occur adjacent to the Asian monsoon region during the northern summer and the Australian monsoon region during the southern summer. *Murakami and Matsumoto* [1994] showed that the Asian monsoon region is divided by the boundary over the South China Sea, where relatively dry weather persists. One region is located over the Bay of Bengal and is driven by thermal contrast between the Indian subcontinent and the Indian Ocean. The other is located over the western North Pacific, where the sea surface temperature is highest in the world, and is mainly driven by asymmetry in sea surface temperatures over the South China Sea and the western North Pacific. The Australian monsoon is located over northern Australia and mainly established by thermal contrast between the Australian continent and the Arafura Sea [*Hung and Yanai*, 2004, and references therein].

El Niño-Southern Oscillation (ENSO) is one of the most dominant interannual variations in the tropical atmosphere and ocean. Its effect is maximum during the southern summer, involving migration of convective activities [e.g. *Yulaeva and Wallace*, 1994; *Gettelman et al.*, 2001], which are stronger in La Niña years located over the western North Pacific than in El Niño years located over the eastern Pacific. During the northern summer, however, ENSO in the previous winter or spring affects convective activities adjacent to the Southeast Asia monsoon in the northern early summer [*Kawamura et al.*, 2001a] and to the North Pacific monsoon region throughout the northern summer [*Kawamura et al.*, 2001b] via the response of sea surface temperatures over the Indian Ocean.

The tropopause temperature could be also affected by the ENSO cycle. During the El Niño phase, tropopause temperatures are fairly uniform; therefore, distribution of water vapor mixing ratios around the tropical tropopause is more zonally uniform than that during the La Niña phase [*Fueglistaler and Haynes*, 2005]. *Gettelman et al.* [2001] and *Fueglistaler and Haynes* [2005] reported that minimum and average tropopause temperatures do not significantly change in connection with the ENSO cycle, but strong El Niño rather than La Niña conditions create moistening.

In this study, we establish an index representing tropopause temperatures forming the horseshoe-shaped structure and examine its relationship with convective activities. Data sets used in this study are described in Section 2. In Section 3, we show general characteristics of the tropical tropopause temperatures. We first define two preliminary indices in Section 4, by focusing on the temperature field characteristics of the Matsuno-Gill pattern. In Section 5, by combining these two indices, we define the index for the horseshoe-shaped structure. Variability in the horseshoe-shaped structure index and its relationship with convective activities are investigated for seasonal and interannual time scales in Sections 6 and 7, respectively. Finally, Section 8 summarizes and concludes this paper.

2. Data

To investigate seasonal and interannual variations in the tropical tropopause temperatures, we used the monthly mean ERA-40 data [*Uppala et al.*, 2005] at 100 hPa with a spatial resolution of 2.5° longitude by 2.5° latitude. We used this data from January

1979 to August 2002 (end of the ERA-40 data period) because improved satellite irradiance data were assimilated during this period. *Fueglistaler and Haynes* [2005] reported that the monthly mean ERA-40 data for tropical tropopause temperatures during that period agree well with radiosonde temperature data and capture the low temperatures much better than those in NCEP reanalyses. They also found an obvious cold bias in the ERA-40 data with respect to radiosondes at the tropical tropopause of about 1-2 K during 1979-85, and about 1 K during 1986-87. However, this discovery is not vital to this study because we focus chiefly on spatial differences such as those calculated in Section 4.1.

As a proxy for convective activities over the tropical region, we used monthly mean OLR data obtained from the National Oceanic and Atmospheric Administration (NOAA) satellites [*Gruber and Krueger*, 1984] from January 1979 to August 2002, the same period as that used for the temperature data, with a spatial resolution of 2.5° longitude by 2.5° latitude. In addition, to assess the effect of ENSO signals on interannual variability in tropical tropopause temperatures, we included the Southern Oscillation index (SOI) as a measure of ENSO status. The SOI data were obtained from the Climate Prediction Center web site http://www.cpc.ncep.noaa.gov/ and were calculated as the difference between sea level pressures in Tahiti (18°S, 150°W) and Darwin (12°S, 131°E).

3. General Characteristics of Tropical Tropopause Temperatures

The horizontal distribution of monthly mean temperatures at 100 hPa and OLR ($\leq$ 220 W/m^2) in August 1995 and February 1984 is shown in Figures 1a and 1b, respectively. The tropopause temperatures during the northern and southern summers have previously been illustrated by using radiosonde data [*Newell and Gould-Stewart*, 1981] and reanalysis data

[*Highwood and Hoskins*, 1998; *Hatsushika and Yamazaki*, 2001]. Tropical temperatures are higher in the northern summer (Figure 1a) than in the southern summer (Figure 1b), resulting from the annual cycle of tropopause temperatures [*Seidel et al.*, 2001]. We choose the two cases, August 1995 and February 1984, for the following reasons: 1) They are neutral-ENSO years, and 2) they are typical examples that show low temperatures extending to the north-west and south-west toward the subtropics to form a horseshoe-shaped structure.

In Figure 1a for the northern summer, low temperatures are located in the Western Pacific around the equator, in the Arabian Sea and South Asia in the northern subtropics around 15°N, and north of the Australian continent in the southern subtropics around 10°S. These low temperatures form the horseshoe-shaped structure. Consistent with *Nishi et al.* [2010], isolated high temperatures are located around the equator between 45°E and 90°E, surrounded by the horseshoe-shaped temperature structure.

A strong convective area (low OLR) for the northern summer (Figure 1a) is located between ∼75°E and 150°E in the Northern Hemisphere. *Murakami and Matsumoto* [1994] divided this convective area into two regions on the basis of different mechanisms of development of the two monsoon systems. One is known as the South Asian monsoon (SoAM) region in the Bay of Bengal, and the other is the North Pacific monsoon (NPM) region in the Western Pacific. The two centers of the convective areas are located around 90°E and 15°N for the SoAM region and around 135°E and 10°N for the NPM region (Figure 1a). This feature is further examined in Figure 5, which shows a longitude-time section of the tropical (20°S-20°N) mean OLR.

In Figure 1b for the southern summer, low temperatures are located in the Western Pacific around the equator and in the northern and southern subtropics around 15°N and 15°S between 90°E and 120°E, forming the horseshoe-shaped structure. Convective activities are present in the Southern Hemisphere adjacent to the Australian monsoon (AUM) region between ∼90°E and 150°E.

A comparison of temperature and OLR distributions during the Southern Hemisphere monsoon season with those during the Northern Hemisphere monsoon season reveals that the horseshoe-shaped structure during the Northern Hemisphere monsoon season is distributed more widely in the longitude and is accompanied by the two convective areas, as mentioned previously. The horseshoe-shaped structure present during the southern summer is similar to that observed in a simulation result for the tropopause temperature with a single idealized heating shown by *Highwood and Hoskins* [1998]. Hence, we propose a concept that the two convective areas during the northern summer result in such a wide distribution of the low temperatures that the horseshoe-shaped structure forms.

4. Variability in Horseshoe-shaped Structure

4.1. Definition of Two Indices

Figure 2 shows a schematic illustration of the horseshoe-shaped temperature structure, which resembles a stationary wave response known as the Matsuno-Gill pattern [*Matsuno*, 1966; *Gill*, 1980], which consists of the Rossby response in the western part and the Kelvin response in the eastern part. Therefore, we first define two indices, HSI-R and HSI-K, as representing longitude-time variations in the Rossby and Kelvin responses, respectively. Then, in Section 5, we further define the integrated index from these two indices to investigate longitude-time variations in the horseshoe-shaped temperature structure.

As a representative of the Rossby response, the index HSI-R is calculated by a curvature of the 100 hPa temperature along the meridional circle at the equator and is given as a function of longitude x and time t:

$$\text{HSI-R}(x,t) = \frac{T_N(x,t) + T_S(x,t)}{2} - T_{Eq}(x,t),$$

where $T_{Eq}(x,t)$ is the temperature at the equator, and $T_N(x,t)$ and $T_S(x,t)$ are temperatures in the subtropics in the Northern and Southern Hemispheres, respectively. The latitude bands for $T_N(x,t)$ and $T_S(x,t)$ are defined as an average between 10°N and 15°N and between 10°S and 15°S, respectively, because we detected that low temperatures representative of the Rossby response are mostly located around these latitudes by checking the 100 hPa temperature data in every month. When low temperatures occur in the subtropics as the Rossby response, this index becomes negative.

As a representative of the Kelvin response, the index HSI-K is calculated by a zonal gradient of the 100 hPa temperature along the equator and is given as a function of longitude x and time t:

$$\text{HSI-K}(x,t) = T_{Eq}(x + \Delta x/2, t) - T_{Eq}(x - \Delta x/2, t).$$

When the temperature structure represents of the Kelvin response, this index becomes negative. A differentiation length, Δx, is set at 20° longitude. A visual inspection of Figure 1 indicates that this length is sufficiently large to detect the Kelvin response and to eliminate effects of small-scale features.

In the horseshoe-shaped structure, negative values of HSI-K are located slightly to the east of the negative values of HSI-R (Figure 2), which is in agreement with the Matsuno-Gill pattern [*Matsuno*, 1966; *Gill*, 1980]. In addition, the two indices may change accordingly with a positive correlation in response to heating generated by convective activities adjacent to monsoon areas.

4.2. Climatological Features

Figures 3, 4, and 5 show longitude-time sections of the HSI-R, HSI-K, and OLR averaged over 23 years during 1979-2002 for each month, respectively, revealing their climatological features. We averaged OLR values between 20°S and 20°N to include the monsoon regions located in the subtropics (Figure 1).

In general, values of both HSI-R and HSI-K are negative and those of OLR are low in the Eastern Hemisphere. These values show similar clear seasonal cycles of strong negative (low) values during the northern and southern summers. As expected from the definition of the two indices mentioned in Section 4.1, negative HSI-K peaks are located east of negative HSI-R peaks. Hence, the horseshoe-shaped structure frequently appears in the Eastern Hemisphere during the northern and southern summers. The longitudinal phase relationship between HSI-R and HSI-K is surveyed in detail in Section 4.3.

In the Western Hemisphere, where values of HSI-R are always positive, two maxima of HSI-R occur from November to May: one is located between 160°W and 75°W, and the other is between 45°W and 0°W. At the western and eastern sides of the two HSI-R maxima, values of HSI-K are positive and negative, respectively. This feature in the Western Hemisphere corresponds to the narrow latitudinal extents of the cold tropical tropopause around 120°W and 30°W (Figure 1b).

Regarding the horseshoe-shaped structure, the negative HSI-R values in the Eastern Hemisphere (Figure 3) are strong in two seasons, as previously mentioned. One occurs during the northern summer from June to October over a large area between 30°E and

150°E, and the other occurs during the southern summer from December to March over a narrow area between 90°E and 120°E; the former is much stronger than the latter. As detailed in Figure 5, the two monsoon regions with low OLR present in the Eastern Hemisphere during the northern summer are distinctly separated around 120°E. Correspondingly, two peaks occur in the negative HSI-R values during the northern summer. The stronger peak is at 70°E in August, at which time and place the isolated warm anomaly on the equator is located (Figure 1a). The weaker peak is at 120°E in August. During the southern summer, a weaker negative peak occurs in HSI-R around 105°E in February rather than that during the northern summer.

In Figure 4, strong negative HSI-K values occur in the Eastern Hemisphere for two seasons. They are similar to those in negative HSI-R values shown in Figure 3. One strong negative values occur during the northern summer from May to September and is situated over a wide area between 60°E and 180°E. Similar to that exhibited by HSI-R and OLR in Figures 3 and 5, respectively, two peaks appear in the longitude. The western peak is stronger and is located around 85°E in July, at which time and place the eastern edges of the isolated warm anomaly on the equator appear, and the eastern peak is around 145°E in August. The other strong negative value occurs during the southern summer from November to March and is located over a narrow area between 100°E and 150°E, and its peak is located around 120°E in December.

Figure 5 shows active convective areas with low OLR between 60°E and 180°E during the northern and southern summers, at which time and place strong negative values occur in HSI-R and HSI-K (Figures 3 and 4, respectively). These convective activities are expected to be located adjacent to the monsoon areas in the Northern Hemisphere during the northern summer and in the Southern Hemisphere during the southern summer. During the northern summer from May to October, low OLR values are divided by the boundary around 120°E, as shown in Figure 1a. The western side is located adjacent to the SoAM region, with its peak around 90°E in July, and the eastern side is adjacent to the NPM region, with its peak around 150°E in August. During the southern summer from December to February, low OLR values are located between 105°E and 150°E adjacent to the AUM region with its peak around 140°E in February. These results agree well with *Murakami and Matsumoto's* [1994] previous study on convective activities over these three monsoon areas. The relationship between the horseshoe-shaped structure and convective activities in the monsoon domains is surveyed in Section 6.

4.3. Longitudinal Phase Lag between HSI-R and HSI-K

As expected from the definition of the two indices stated in Section 4.1, the negative HSI-K peaks should be located east of the negative HSI-R peaks. The longitudinal phase lag α is examined in Figure 6 through calculation of the correlation coefficients between the monthly mean values of HSI-R(x, t) and HSI-K$(x + \alpha, t)$ in the Eastern Hemisphere $(0° \leq x < 180°)$, where they are mostly negative (Figures 3 and 4). The longitudinal phase lag that provides the most significant correlation differs somewhat in the four seasons and is smaller in the southern summer than in the northern summer (Figure 6). This result could be explained by the concept that the horseshoe-shaped structure during the northern summer is zonally more elongated than that during the southern summer because the convective area during the former is zonally more extended than that during the latter (Figure 1). The correlation coefficient for all months is most significant ($r = 0.52$) when the phase lag is $+15.0°$ and the correlation coefficient for each season is around 0.5-0.6.

Therefore, we set the longitudinal phase lag of HSI-K relative to HSI-R at $+15.0°$ in the following analysis.

5. Integrated Index

In this section, we define the index representing the horseshoe-shaped temperature structure using HSI-R and HSI-K values in the Eastern Hemisphere. Figures 7 shows a frequency distribution of the monthly mean values of HSI-R and HSI-K in the Eastern Hemisphere from January 1979 to August 2002. Here we set the longitudinal phase lag of $+15.0°$ for HSI-K relative to HSI-R. We performed an empirical orthogonal function (EOF) analysis with the covariance matrix of HSI-R and HSI-K in the Eastern Hemisphere. The red solid line in Figure 7 represents the first basis function, hereafter termed HSI-1(x,t), accounting for 79.2% of the total variance; HSI-1$(x,t) = 0.618 \times$ HSI-K$(x + 15°, t) + 1.12 \times$ HSI-R(x,t). This function features a positive linear relation between HSI-R and HSI-K values, and is negative when both values are negative. Therefore, when the HSI-1 value is negative, the temperature field should be representative of the horseshoe-shaped structure. The second basis function, hereafter termed HSI-2(x,t), is indicated in Figure 7 as a red dashed line, accounting for 20.8% of the total variance; HSI-2$(x,t) = 0.57 \times$ HSI-K$(x + 15°, t) - 0.317 \times$ HSI-R(x,t).

6. Seasonal Variability adjacent to Monsoon Regions

Figure 8 shows longitude-time sections similar to that indicated in Figure 3, but for HSI-1 and HSI-2 in the Eastern Hemisphere. The seasonal variation in HSI-1 value (Figure 8a) is almost similar to that in the climatological HSI-R and HSI-K values in the Eastern Hemisphere (Figures 3 and 4, respectively). Negative HSI-1 values are strong during the northern summer between 45°E and 150°E and are distinctly separated by the boundary around 110°E. The western area peaks in July at 70°E, where the isolated warm anomaly on the equator appears. The eastern area peaks around 120°E in August. During the southern summer between 90°E and 120 °E, a strong negative HSI-1 area occurs with a peak around 105°E in February.

The seasonality of the negative HSI-1 also shows a good correspondence to that of the climatological OLR values in the SoAM, NPM, and AUM regions (Figure 5), which are located about 10°-20° degrees east of the negative HSI-1 values. Figure 9 shows scatterplots of the OLR and HSI-1 values averaged over 23 years for each month over the (a) SoAM, (b) NPM, and (c) AUM domains, which are selected as summarized in Table 1. Strong positive correlations between the OLR and HSI-1 values occur during May-December in the SoAM and NPM domains and during November-April in the AUM domain. Hence, we can conclude that the seasonal cycle in the horseshoe-shaped structure is clearly related to convective activities over the three monsoon domains.

As shown in Figure 8b, HSI-2 values are positive west of the negative HSI-1 peaks, with the most extreme located over 30°E-60°E during June-September. This result could refer to the western edges of the isolated high temperatures at the equator, which are surrounded by temperatures with the horseshoe-shaped structure, because an HSI-2 value can be positive when an HSI-R value is negative and an HSI-K value is positive (Figure 7). In fact, the climatological HSI-R and HSI-K values over 30°E-60°E during the northern summer are negative and positive, respectively (Figures 3 and 4).

7. Interannual Variability and its Link to ENSO

In the previous section, it was shown that the seasonal variation in HSI-1 for each of the three monsoon regions is clearly related to the corresponding convective activities indicated by the OLR values. In this section, we examine interannual variation in HSI-1 such as that due to the ENSO cycle. The ENSO effect is expected to be maximum during the southern summer, involving migration of convective activities over the Pacific [e.g., *Yulaeva and Wallace*, 1994; *Gettelman et al.*, 2001]. On the other hand, during the northern summer, strong convective activities adjacent to the monsoon regions are robust features, therefore, ENSO may not necessarily directly affect interannual variation in convective activity and HSI-1. In the following section, we first investigate the cases during the northern summer for the SoAM and NPM domains, then during southern summer when the AUM domain is highly affected. For the latter analysis, to capture the migration in association with ENSO, we extend our analysis in the longitudinally-moving frame of HSI-1 and OLR.

7.1. Northern Summer

Figure 10 shows scatterplots of OLR and HSI-1 values averaged over the (a) SoAM and (b) NPM domains over July-August for each year. In these two months, the climatological HSI-1 in each of the monsoon domains reaches its negative peak (Figures 9a and 9b). The correlation coefficient is significant in the NPM domain, suggesting that the HSI-1 value is affected by convective activities even in the interannual time scale, but not in the SoAM domain.

Kawamura et al. [2001b] showed that in the NPM area, interannual variation in convective activity is related to the ENSO signal in the previous winter via the response of sea surface temperatures over the Indian Ocean. In fact, the lag correlation coefficient between the OLR values averaged over July-August in the NPM domain and the SOI values averaged over January-February in the same year is −0.54, higher than the simultaneous correlation coefficient of 0.24 (neither shown). Hence, the lag correlation coefficient between the HSI-1 values in the NPM domain and the SOI values in the previous winter is significant (−0.49) (Figure 11b).

In the SoAM domain, although the relationship with convective activities is not evident (Figure 10a), the simultaneous correlation coefficient between SOI and HSI-1 values (Figure 11a) is significant. To examine the interannual variability in the SoAM domain in detail, we composed distributions of temperature at 100 hPa and OLR during July-August for two cases. The first (Figure 12a) is for a "strong" case reflecting a strongly negative HSI-1 value in the SoAM domain (1988 and 1991); the second (Figure 12b) is for a "weak" case reflecting an HSI-1 value of nearly zero (1982, 1987, 2001, and 2002). Because the strong and weak cases are comparable with the La Niña and El Niño years, respectively, the lowest temperature area at the equator is located over the western Pacific for the strong case and shifts eastward around 160°W for the weak case, which is in agreement with the composite difference between the El Niño and La Niña years during the northern summer presented by *Hatsushika and Yamazaki* [2001]. We detected that strong negative HSI-1 values in the SoAM domain during July-August indicate prominent warm anomalies around 60°E surrounded by the horseshoe-shaped temperature structure.

Nishi et al. [2010] reported that strength in the warm anomalies is weak in the strong El Niño years, which agrees with our results, although they did not show the relationship with convective activities. In addition, the researchers suggested that tropical easterly winds, which are part of an anticyclonic circulation over the Tibetan Plateau in the upper troposphere and the lower stratosphere, can relate to the intensity of the warm anomalies. The anticyclone could be maintained by sensible heating over the Tibetan Plateau, and the intensity of the anticyclone varies with the life cycle of ENSO [*Hoskins and Wang*, 2006]. However, the mechanism of formation and variability of the warm anomaly remains to be discussed.

7.2. Southern Summer

A correlation coefficient between OLR and HSI-1 values averaged over the AUM domain (i.e., the longitudinally-fixed frame) over January-February for each year is significant at 0.83 (not shown). However, convective activities over the Pacific migrate with the ENSO cycle during the southern summer [e.g. *Yulaeva and Wallace*, 1994; *Gettelman et al.*, 2001]; therefore, the relationship between OLR and HSI-1 values in the longitudinally-moving frame was examined further.

Figure 13 shows the relationship between longitudes of OLR and HSI-1 minima in each year. These OLR and HSI-1 values are averaged over January-February, and the OLR values are further averaged over 15°S-10°N and smoothed by a running mean for 42.5° longitude. We detected that the HSI-1 minima are located around 100°E-120°E in most years, accompanied by OLR minima around 110°E-150°E; these regions correspond to the AUM area as summarized in Table 1. In some years, the HSI-1 minima move to the east of 135°E; these years are basically in the El Niño phase. The longitudinal phase difference between HSI-1 and OLR is larger as the minima shift eastward. This relation is significant with a correlation coefficient of 0.91, except for the case in January-February 1990, marked by a red dot. *Hayes et al.* [1991] and *Bergman et al.* [2001] reported that although early stages of El Niño development were evident in February 1990, El Niño did not develop fully after that time. Figure 14 reveals a positive correlation between the OLR and HSI-1 minima in the longitudinally-moving frame; the case in January-February 1990 is omitted.

Figure 15 displays composite maps for the strong and weak cases, similar to that shown in Figure 12. In Figure 15a, the strong case represents years when the HSI-1 minimum in the moving frame during January-February is strongly negative (1984, 1996, and 2000), and Figure 15b shows the weak case representing years at nearly zero (1983, 1988, and 1993). Because those years for the strong and weak cases are in La Niña and El Niño phases, respectively, the following features in the composites are consistent with those for the El Niño and La Niña years in both the tropopause temperature [*Hatsushika and Yamazaki*, 2001] and convective activities [*Yulaeva and Wallace*, 1994; *Gettelman et al.*, 2001]. For the strong case (Figure 15a), low temperatures form the horseshoe-shaped structure over the Western Pacific, surrounding warm anomalies on the equator around 110°E, and strong convective activities occur over the Australian monsoon region. For the weak case (Figure 15b), the low temperature region shifts eastward, and its shape becomes zonally elongated and meridionally narrow, similar to that observed in convective activities.

7.3. Variation in Minimum Temperature

From the composite temperature fields for the two cases as shown in Figures 12 and 15, we found that minimum tropopause temperatures over 15°N-15°S do not differ significantly between the strong and weak cases. For the northern summer, these temperatures are 194.8 K and 193.2 K in the SoAM domain and 194.0 K and 194.1 K in the NPM domain; the respective southern summer temperatures are 189.4 K and 190.6 K. These results agree with previous studies that surveyed the effect of ENSO on a dehydration process [*Gettelman et al.*, 2001; *Fueglistaler and Haynes*, 2005]. However, *Gettelman et al.* [2001] used a water vapor mixing ratio measured from the Halogen Occultation Experiment (HALOE) and concluded the following factors. Strong El Niño conditions (in this study, the weak case for the northern summer in the SoAM domain and for the southern summer) have a moistening impact on the water vapor mixing ratio of air entering the stratosphere, while La Niña conditions (in this study, the strong case for the northern summer in the SoAM domain and for the southern summer) have a drying impact. Their results agree with AGCM simulations reported by *Hatsushika and Yamazaki* [2003] and *Scaife et al.* [2003] and with the Lagrangian calculations of troposphere-to-stratosphere transport based on ERA-40 temperatures reported by *Fueglistaler and Haynes* [2005]. As *Holton and Gettelman* [2001] and *Hatsushika and Yamazaki* [2003] showed the importance of the horizontal wind circulation in the dehydration process, this discrepancy would account for the strength in the atmospheric circulation accompanied by the horseshoe-shaped structure such as that expressed by the HSI-1 values.

8. Summary and Conclusion

We have established the index representing a zonally asymmetric temperature structure in the tropical tropopause, and investigated its variability associated with convective activity using ERA-40 and NOAA/OLR data. Particularly during the northern and southern summers, low temperatures persist over the tropics and extend north-west and south-west. These low temperatures form a horseshoe-shaped structure that resembles the Matsuno-Gill pattern, which consists of the Rossby response in the western part and the Kelvin response in the eastern part.

Regarding the horseshoe-shaped structure, we defined two preliminary indices. As a representative of the Rossby response, an index HSI-R(x, t) was calculated from a curvature of the 100 hPa temperature along the meridional circle at the equator; as a representative of the Kelvin response, an additional index HSI-K(x, t) was calculated from a zonal gradient of the 100 hPa temperature along the equator. The two indices were then integrated into one index HSI-1 as a result of the EOF analysis using HSI-R and HSI-K values. The index HSI-1 projected a positive linear relation between HSI-R and HSI-K; hence, its negative value should suggest clear existence of the horseshoe-shaped temperature structure.

The negative value of HSI-1 is frequently observed in the Eastern Hemisphere, and its seasonal cycle is closely related to convective activities adjacent to the monsoon areas, including the SoAM and NPM domains during the northern summer and the AUM domain during the southern summer. Convective activities in the SoAM and NPM domains may induce two horseshoe-shaped structures individually, and a superposition of the two structures can produce a longitudinally elongated horseshoe-shaped structure during the northern summer.

The ENSO cycle was shown to greatly affect variations in HSI-1 values and convective activities, particularly during the southern summer. As discussed in previous studies [*Yulaeva and Wallace*, 1994; *Hatsushika and Yamazaki*, 2001; *Gettelman et al.*, 2001], low temperatures form the horseshoe-shaped structure over the equator in the Western Pacific during the southern summer for the non-El Niño years, while low temperatures shift eastward and becomes more zonally elongated and meridionally narrow for the El Niño years. The longitudinal phase difference between the OLR and HSI-1 minima in the El Niño years is larger than that observed in the non-El Niño years.

During the northern summer, the interannual variability in HSI-1 in the NPM domain is affected by the ENSO cycle in the previous winter, which is consistent with a previous study on convective activities in the NPM area [*Kawamura et al.*, 2001b]. In the SoAM domain, interannual variation in HSI-1 values is not significantly related to convective activities in the monsoon domain. We detected that the HSI-1 value in the SoAM domain is mainly controlled by the isolated high temperatures observed around 60°E over the equator during July-August, which are surrounded by the horseshoe-shaped structure. The interannual variation in the HSI-1 values is related to the ENSO cycle, which agrees with a previous study on the isolated high temperatures reported by *Nishi et al.* [2010]. The variation in the high temperature may be related to an anticyclone in the upper troposphere over the Tibetan Plateau. However, further discussion is necessary on the detailed mechanism of formation and variability of the isolated high temperatures.

This study clearly revealed the seasonal and interannual variability of the temperature structure around the tropical tropopause and its relationship with convective activities over the monsoon regions with respect to the horseshoe-shaped temperature structure. Relations to shorter time scale oscillations such as intraseasonal oscillation, traveling Kelvin waves and active/break cycles in the Asian monsoon circulation are interesting topics for further investigation. Moreover, numerical experiments are required to validate the use of the index representing the horseshoe-shaped temperature field with respect to convective activities.

Acknowledgments. We thank Dr. N. Nishi of Kyoto University for helpful discussions throughout this work. Data analysis and visualization were done using libraries developed by the GFD-DENNOU Ruby project (http://ruby.gfd-dennou.org/).

References

Bergman, J. W., H. H. Hendon, and K. M. Weickmann (2001), Intraseasonal Air-Sea Interactions at the Onset of El Niño, *J.Climate*, *14*(8), 1702–1719, doi:10.1175/1520-0442(2001)014¡1702:IASIAT¿2.0.CO;2.

Dima, I. M., and J. M. Wallace (2007), Structure of the Annual-Mean Equatorial Planetary Waves in the ERA-40 Reanalyses, *J. Atmos. Sci.*, *64*(8), 2862–2880, doi: 10.1175/JAS3985.1.

Fueglistaler, S., and P. H. Haynes (2005), Control of interannual and longer-term variability of stratospheric water vapor, *J. Geophys. Res.*, *110*, D24,108, doi: 10.1029/2005JD006019.

Fueglistaler, S., A. E. Dessler, T. J. Dunkerton, I. Folkins, Q. Fu, and P. W. Mote (2009), Tropical tropopause layer, *Rev. Geophys.*, *47*(1), RG1004, doi:10.1029/2008RG000267.

Gettelman, A., W. J. Randel, S. Massie, F. Wu, W. G. Read, and J. M. Russell (2001), El Niño as a Natural Experiment for Studying the Tropical Tropopause Region, *J. Climate.*, *14*(16), 3375–3392.

Gill, A. E. (1980), Some simple solutions for heat-induced tropical circulation, *Q. J. R. Meteorol. Soc.*, *106*(449), 447–462.

Gruber, A., and A. F. Krueger (1984), The Status of the NOAA Outgoing Longwave Radiation Data Set, *Bull. Am. Meteorol. Soc.*, *65*(9), 958–962.

Hartmann, D. L. (2007), The Atmospheric General Circulation and Its Variability, *J. Meteor. Soc. Jpn.*, *85B*, 123–143.

Hatsushika, H., and K. Yamazaki (2001), Interannual variations of temperature and vertical motion at the tropical tropopause associated with ENSO, *Geophys. Res. Lett.*, *28*(15), 2891–2894, doi:10.1029/2001GL012977.

Hatsushika, H., and K. Yamazaki (2003), Stratospheric drain over Indonesia and dehydration within the tropical tropopause layer diagnosed by air parcel trajectories, *J. Geophys. Res.*, *108*, 4610, doi:10.1029/2002JD002986.

Hayes, S. P., L. J. Mangum, J. Picaut, A. Sumi, and K. Takeuchi (1991), TOGA-TAO: A Moored Array for Real-time Measurements in the Tropical Pacific Ocean, *Bull.Amer.Meteor.Soc.*, *72*(3), 339–347, doi:10.1175/1520-0477(1991)072¡0339:TTAMAF¿2.0.CO;2.

Highwood, E. J., and B. J. Hoskins (1998), The tropical tropopause, *Q. J. R. Meteorol. Soc.*, *124*(549), 1579–1604.

Holton, J. R., and A. Gettelman (2001), Horizontal transport and the dehydration of the stratosphere, *Geophys. Res. Lett.*, *28*(14), 2799–2802, doi:10.1029/2001GL013148.

Hoskins, B. J., and B. Wang (2006), The Asian Monsoon, Chapter 9 Large-Scale Atmospheric Dynamics, *Springer, Chichester, UK.*, *edited by B. Wang,*, pp. 378.

Hung, C.-W., and M. Yanai (2004), Factors contributing to the onset of the Australian summer monsoon, *Q.J.R.Meteorol.Soc.*, *130*(597), 739–758, doi:10.1256/qj.02.191.

Kawamura, R., T. Matsuura, and S. Iizuka (2001a), Role of equatorially asymmetric sea surface temperature anomalies in the Indian Ocean in the Asian summer monsoon and El Niño-Southern Oscillation coupling, *J.Geophys.Res.*, *106*, 4681–4693, doi:10.1029/2000JD900610.

Kawamura, R., T. Matsuura, and S. Iizuka (2001b), Interannual atmosphere-ocean variations in the tropical western North Pacific relevant to the Asian summer monsoon-ENSO coupling, *J. Meteor. Soc. Jpn.*, *79*(4), 883–898.

Kley, D., J. M. R. III, and C. Phillips (Eds.) (2000), *SPARC assessment of upper tropospheric and lower stratospheric water vapor*, WCRI 113, 312 pp., World Meteorol. Organ., Geneva, Switzerland.

Matsuno, T. (1966), Quasi-geostrophic motions in the equatorial area, *J. Meteor. Soc. Jpn.*, *44*(1), 25–42.

Murakami, T., and J. Matsumoto (1994), Summer monsoon over the Asian continent and western North Pacific, *J. Meteor. Soc. Jpn.*, *72*(5), 719–745.

Newell, R. E., and S. Gould-Stewart (1981), A Stratospheric Fountain?, *J. Atmos. Sci.*, *38*(12), 2789–2796.

Nishi, N., E. Nishimoto, H. Hayashi, M. Shiotani, H. Takashima, and T. Tsuda (2010), Quasi-stationary temperature structure in the upper troposphere over the tropical Indian Ocean inferred from radio occultation data, *J. Geophys. Res.*, *115*, D14,112, doi:10.1029/2009JD012857.

Norton, W. A. (2006), Tropical Wave Driving of the Annual Cycle in Tropical Tropopause Temperatures. Part II: Model Results, *J. Atmos. Sci.*, *63*(5), 1420–1431, doi:10.1175/JAS3698.1.

Park, M., W. J. Randel, A. Gettelman, S. T. Massie, and J. H. Jiang (2007), Transport above the Asian summer monsoon anticyclone inferred from Aura Microwave Limb Sounder tracers, *J. Geophys. Res.*, *112*, D16,309, doi:10.1029/2006JD008294.

Randel, W. J., and M. Park (2006), Deep convective influence on the Asian summer monsoon anticyclone and associated tracer variability observed with Atmospheric Infrared Sounder (AIRS), *J. Geophys. Res.*, *111*, D12,314, doi:10.1029/2005JD006490.

Scaife, A. A., N. Butchart, D. R. Jackson, and R. Swinbank (2003), Can changes in ENSO activity help to explain increasing stratospheric water vapor?, *Geophys.Res.Lett.*, *30*(17), 1880, doi:10.1029/2003GL017591.

Seidel, D. J., R. J. Ross, J. K. Angell, and G. C. Reid (2001), Climatological characteristics of the tropical tropopause as revealed by radiosondes, *J. Geophys. Res.*, *106*, 7857–7878, doi:10.1029/2000JD900837.

Uppala, S. M., et al. (2005), The ERA-40 re-analysis, *Q. J. R. Meteorol. Soc.*, *131*(612), 2961–3012.

Yulaeva, E., and J. M. Wallace (1994), The Signature of ENSO in Global Temperature and Precipitation Fields Derived from the Microwave Sounding Unit, *J. Climate.*, *7*(11), 1719–1736.

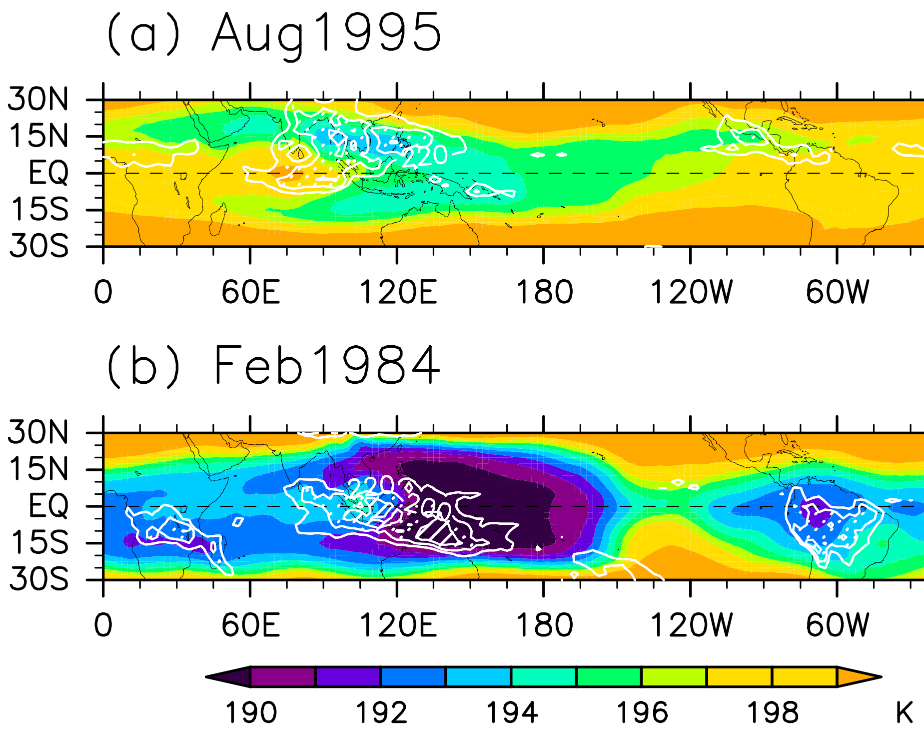

Figure 1. Maps of temperature at 100hPa (K; color) and OLR (W/m^2; white contour) at (a) August 1995 and (b) February 1984. Contours of OLR are drawn only 180, 200 and 220 W/m^2.

Table 1. Domains of HSI-1 and OLR for SoAM, NPM and AUM.

	SoAM	NPM	AUM
HSI-1	60°E-90°E	110°E-150°E	100°E-120°E
OLR	5°N-20°N 70°E-110°E	5°N-20°N 130°E-180°E	15°S-10°N 110°E-150°E

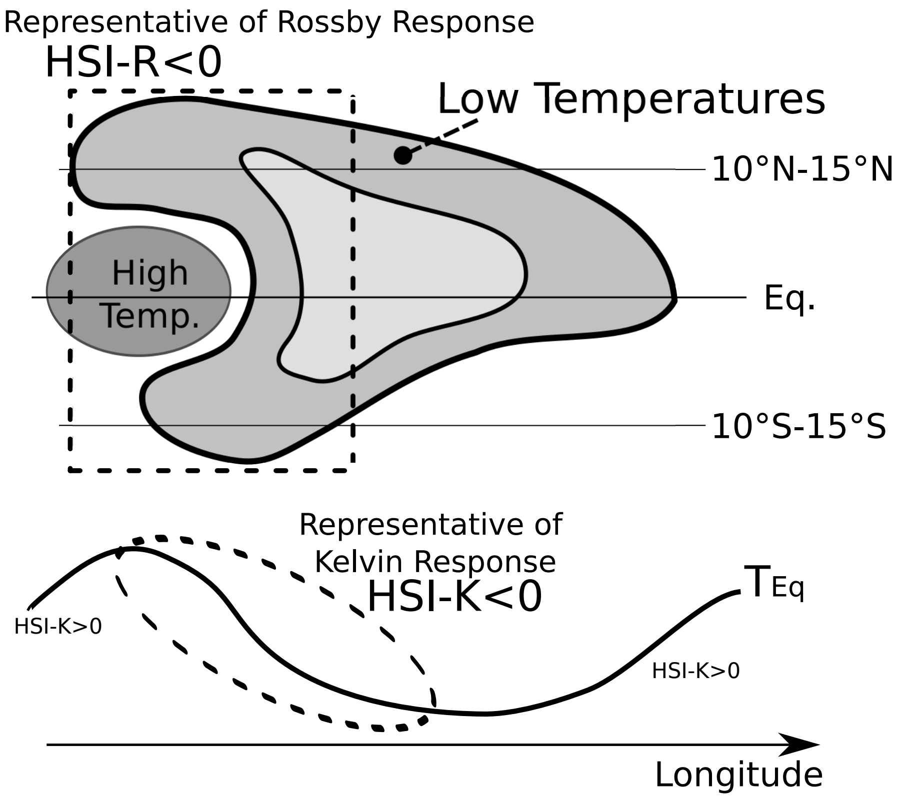

Figure 2. A schematic diagram of the horseshoe-shaped structure and an explanation of HSI-R and HSI-K.

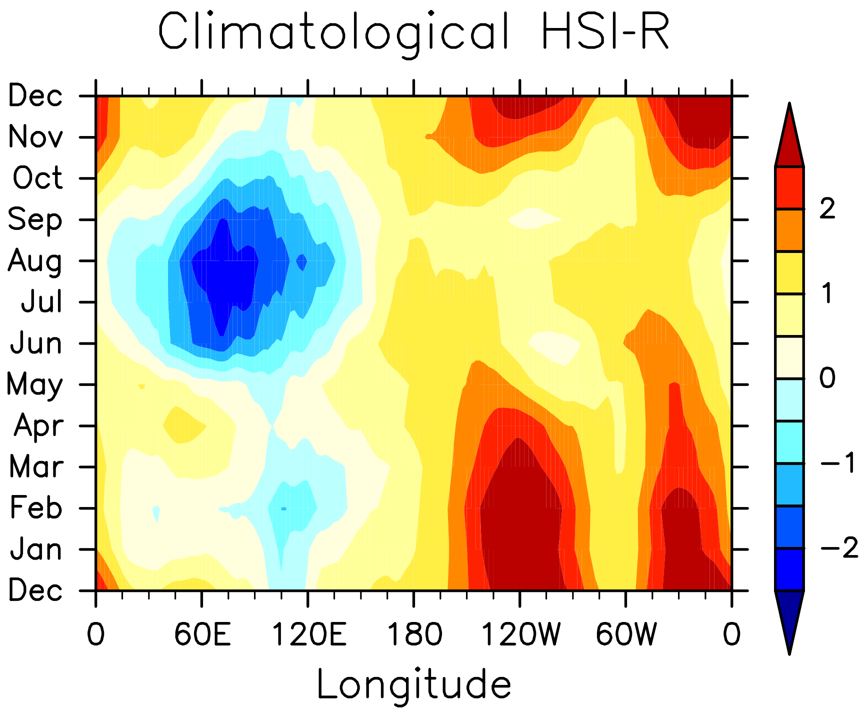

Figure 3. A longitude-time cross section of HSI-R, which represents the Rossby response, averaged over 23 years (1979-2002) at each month.

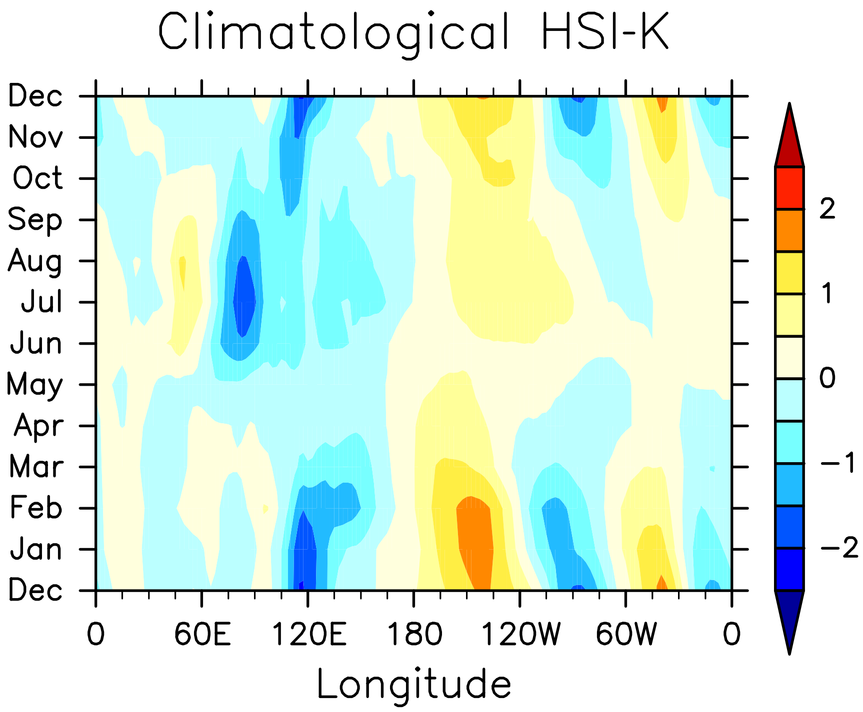

Figure 4. Same as Figure 3, but for HSI-K, which represents the Kelvin response.

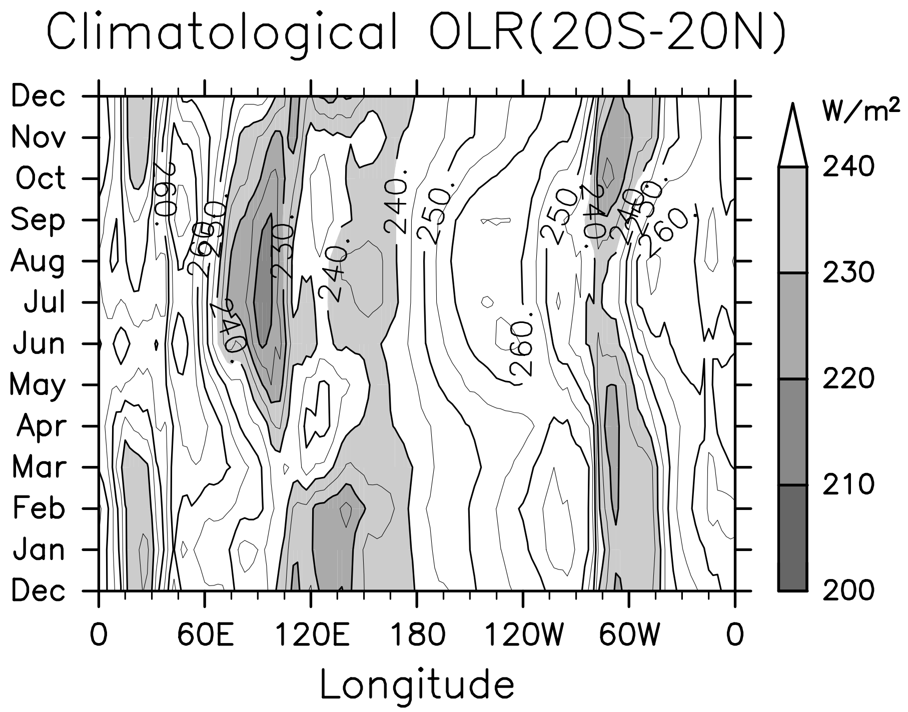

Figure 5. Same as Figure 3, but for tropical (20°S-20°N) mean OLR.

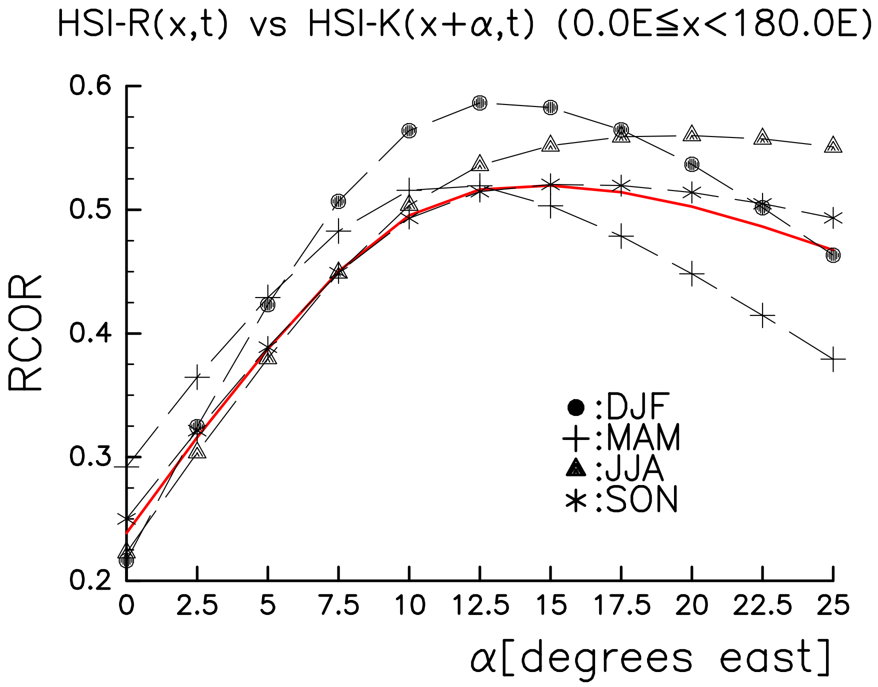

Figure 6. Correlation coefficients between HSI-R and HSI-K in the eastern hemisphere with longitudinal phase lag α for HSI-K relative to HSI-R. Black lines and marks show correlation coefficients calculated using the values in each season, and a red line for all season. The legend of marks are shown in a panel.

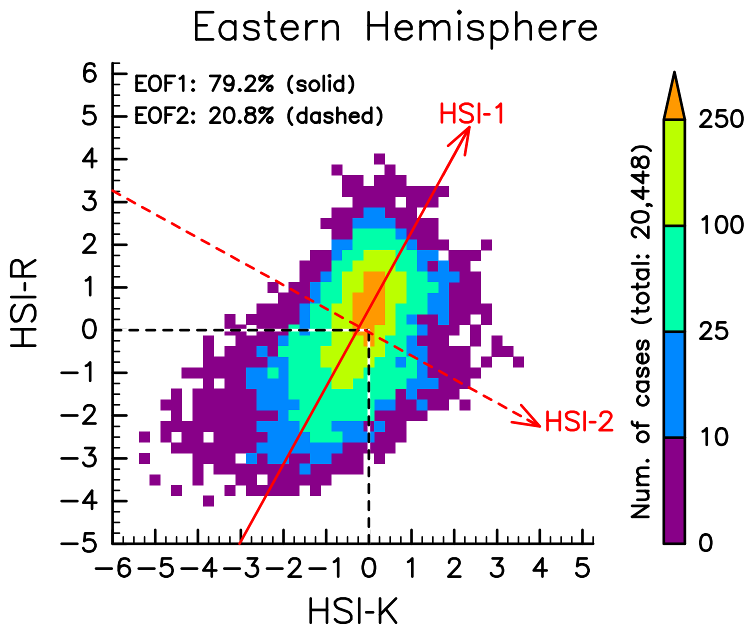

Figure 7. Frequency of occurrence for HSI-K and HSI-R bi-intervals between January 1979 and August 2002 in the Eastern Hemisphere. Red line indicates the linear regression line of the first EOF mode (solid) and the second EOF mode (dashed), which are calculated by using the values in the Eastern Hemisphere.

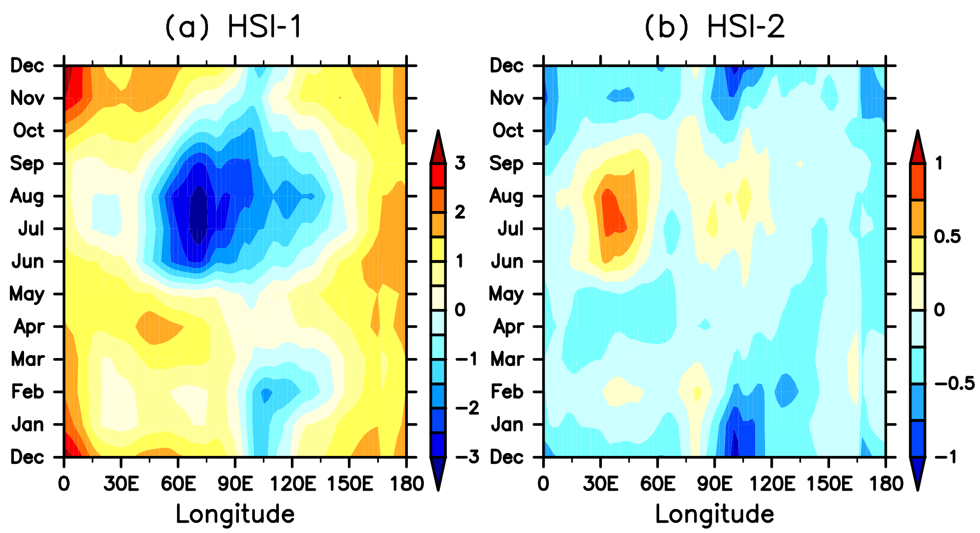

Figure 8. Same as Figure 3, but for (a) HSI-1 and (b) HSI-2 in the Eastern Hemisphere.

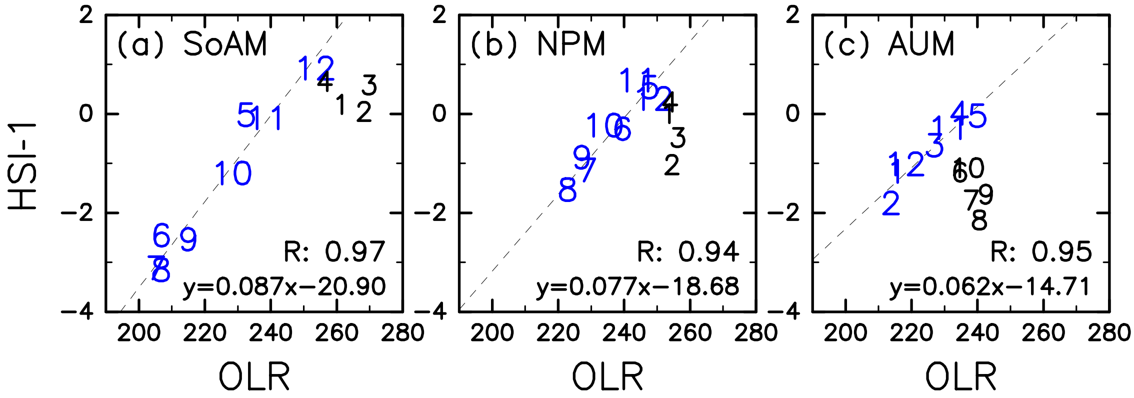

Figure 9. Scatterplots of the climatological OLR and HSI-1 values in the (a) SoAM, (b) NPM and (c) AUM domains. The number on the scatterplots refers to the month of the data. Correlations and regression lines (indicated by dashed lines) are calculated by using data during May-December in the SoAM and NPM domains and during November-April in the AUM domain.

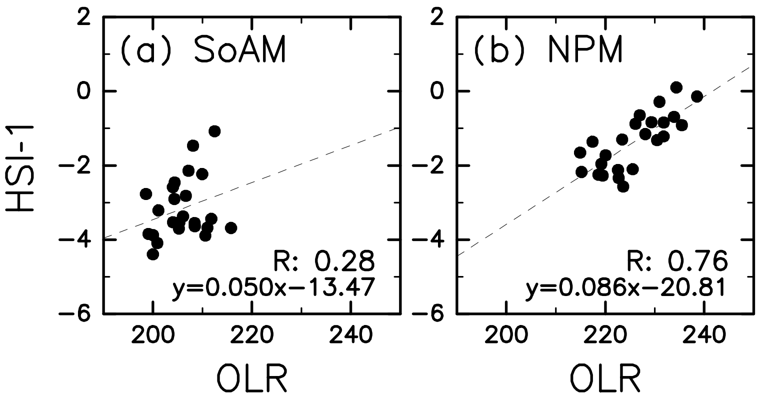

Figure 10. Scatterplots of OLR and HSI-1 values averaged over July-August in the (a) SoAM and (b) NPM domains. Dashed lines indicate linear regression lines.

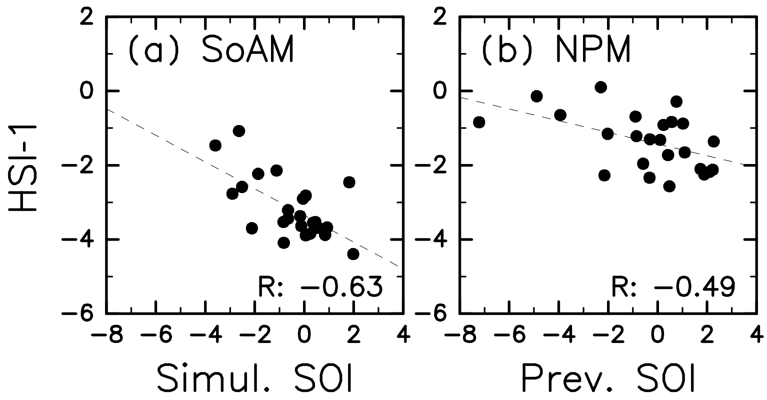

Figure 11. Same as Figure 10, but for (a) SOI values in simultaneous season and HSI-1 values in the SoAM domain and for (b) SOI values in previous winter and HSI-1 values in the NPM domain.

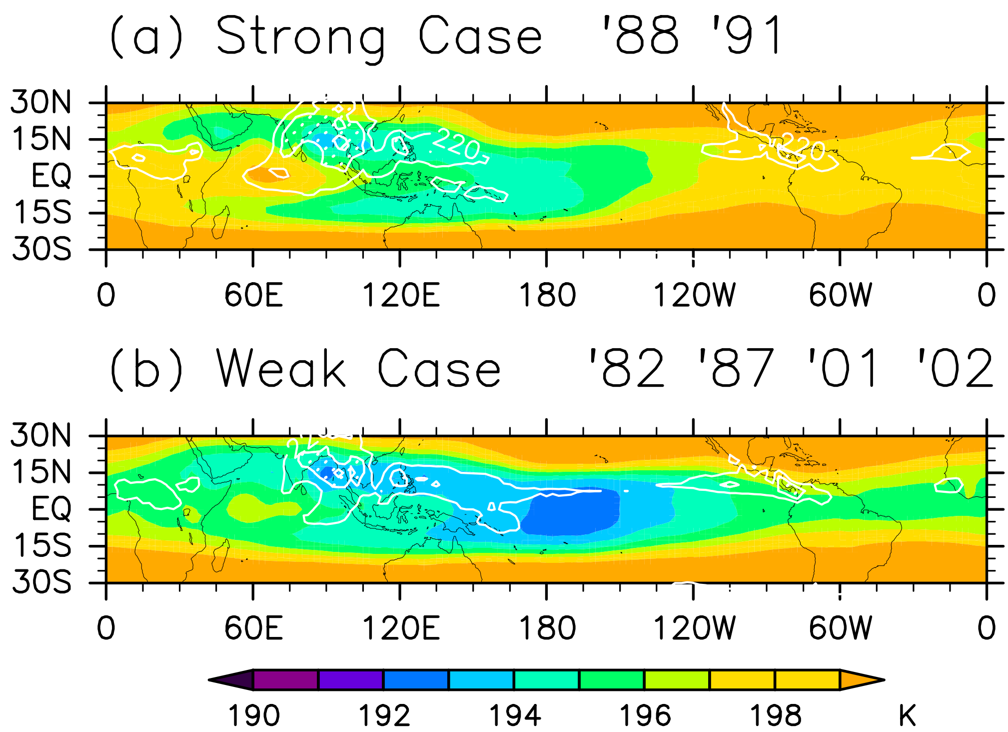

Figure 12. Composite maps of temperature at 100hPa (K; color) and OLR (W/m^2; white contour) for (a) the strong case reflecting a strongly negative HSI-1 value in the SoAM area, and (b) the weak case reflecting an HSI-1 value of nearly zero. OLR contours is drawn only 200 and 220 W/m^2.

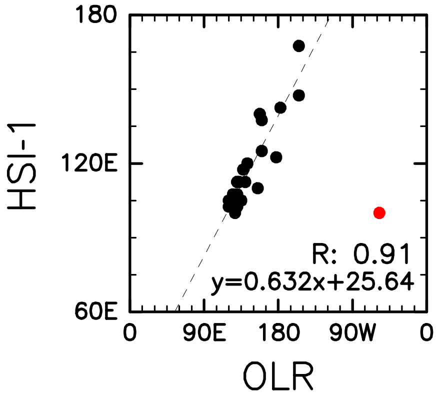

Figure 13. A scatterplot of longitudes of OLR and HSI-1 minima in each year during January-February. A red dot refers to the 1990 case. Correlation and regression line (indicated by dashed lines) are calculated using the values excluding the 1990 case.

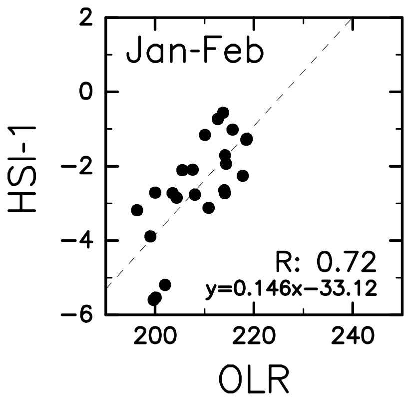

Figure 14. Same as Figure 10, but for OLR and HSI-1 minima in the longitudinally-moving frame during January-February. The 1990 case is omitted.

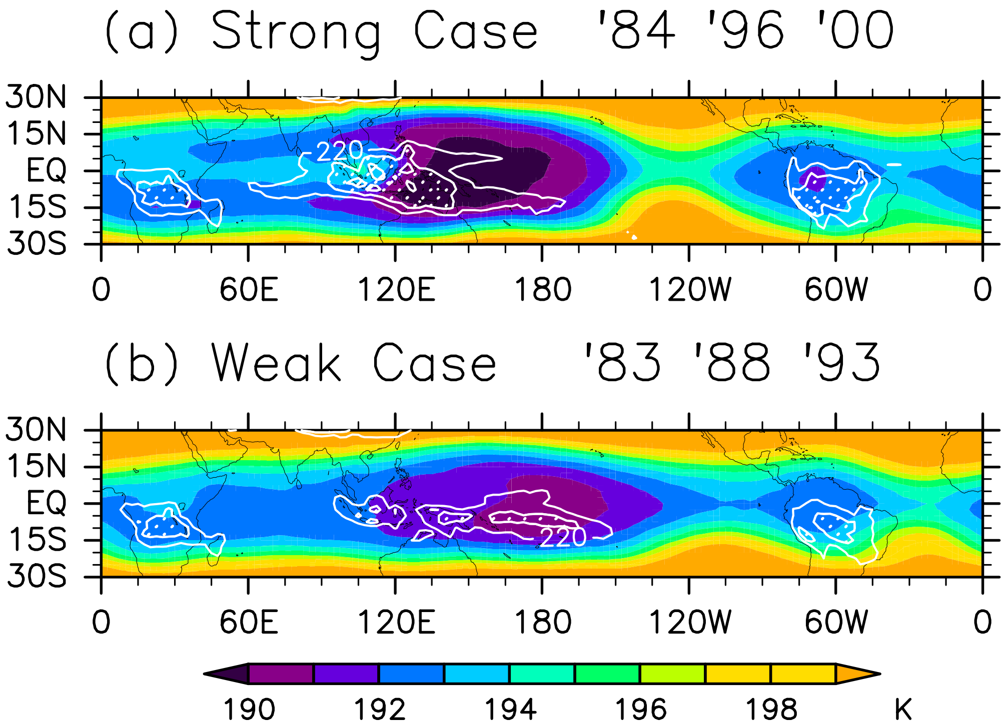

Figure 15. Same as Figure 12, but for (a) the strong case in the longitudinally-moving frame during January-February, and (b) the weak case.